A Software-Based Bandwidth Compensation Method for Small-Resistance Coaxial Current Shunt

Zilong CHEN, Yanjie HE, Yukun ZHANG, and Yuqi WEI

***Abstract*—Due to the increasing switching speed of the wide band gap (WBG) devices, there is an urgent demand for the high-bandwidth current sensor. However, the low bandwidth of the low-resistance coaxial current shunt (CCS) becomes the hindrance to the WBG device characterizations. This paper proposes a low-cost bandwidth compensation method for the low-resistance CCS. Since the structure of the CCS is complicated, it is regarded as a two-port network, and a high-resistance high-bandwidth CCS is used to generate the compensation transfer function. The proposed method is verified by the double pulse test (DPT) of a Gallium Nitride (GaN) device. The maximum errors for the turn-on switching loss and total switching loss after compensation are 1.1% and 1.2%, respectively. While these values before compensations are 35.3% and 31.7%, respectively. In addition, the proposed method is not sensitive to the preselected testing condition, which indicates its high practical engineering value.**

***Index Terms*—Coaxial current shunt resistor, current measurement, GaN device, high bandwidth.**

I. INTRODUCTION

THE wide band gap (WBG) power semiconductor devices have been increasingly used in power converters due to their excellent electrical and thermal characteristics [1], [2]. However, the datasheet provided by the vendor is always obtained from special conditions, which would have a considerable deviation compared with the practical condition [3], [4]. The characterization of WBG semiconductor devices under practical conditions is essential because it is sensitive to parasitic parameters and environmental conditions [5].

The double pulse test (DPT) is a widely used dynamic characterization method. The rise/fall time, the turn-on/off switching loss, and the waveform oscillation can be obtained by DPT. The fast switching speed of WBG devices makes it a great challenge for measurement, which requires probes with a high bandwidth and a large measurement range scale simultaneously [6]. It is more difficult to achieve high bandwidth for current measurement than that of voltage probes [7]. Therefore, the focus of this paper is on the current measurement. The Rogowski coil (RC) current probe, the current transformer (CT), and the current shunt are three generally used methods. Among them, the current transformer can achieve a wide current measurement range. But the large size and additional loop inductance restrict its application on WBG devices [8]. Comparing with the current transformer, the RC current sensor does not introduce much parasitic inductance into circuit and can achieve a wide current measurement range (several hundreds ampere). However, the low bandwidth of the commercial RC restricts the application on WBG device current measurement [9]. Therefore, researchers design kinds of PCB-based RC current sensors to overcome the bottleneck of bandwidth [10]–[12]. It is reported that the bandwidth of the self-designed RC current sensors arrives 100 MHz to 200 MHz in laboratory. There are mainly two issues of the self-designed RC current sensor. One is that the low-frequency bandwidth cannot be guaranteed, the other is that the additional integral circuit design and calibration increase the implementation complexity [12].

The surface mounted device (SMD) current shunt is widely used in the low frequency circuit because the parasitic inductance of it cannot be ignored under the high frequency condition [13]. As a consequence, the coaxial current shunt (CCS) is considered as one of the best choices for its low additional parasitic inductance and relatively high bandwidth [14].

According to [15], the inherent inductance is the main limitation of the CCS bandwidth. As a result, many researchers are making great effort to optimize the inherent inductance of the CCS. However, the inherent inductance value is already so small (e.g., several pH) that further optimization is difficult. This situation is more serious for the low-resistance CCS, as it may need a much smaller inherent inductance than that of the high-resistance CCS to achieve the same bandwidth, which is also explained later. Consequently, the off-the-shelf low-resistance CCS can only achieve a low bandwidth. It is found that the actual bandwidth of the low-resistance CCS is dramatically lower than the nominal bandwidth claimed by the vendor [7]. Therefore, the low-resistance CCS cannot meet the DPT measurement requirement.

In order to obtain a convincing and accurate result, there are mainly three methods. They are using the high-resistance high-bandwidth CCS, compensating the low-resistance CCS and designing a high-bandwidth low-resistance CCS. The drawback of the high-resistance CCS is mainly the limitation

---

Manuscript received August 22, 2025; revised November 18, 2025; accepted December 11, 2025. Date of publication March 30, 2026; date of current version January 13, 2026. This work was supported in part by the National Natural Science Foundation of China under the grant 52307221. (*Corresponding author: Yuqi Wei.*)

All authors are with the State Key Laboratory of Electrical Insulation and Power Equipment, Xi’an Jiaotong University, Xi’an 710049, China (e-mail:czl0928@stu.xjtu.edu.cn; yanjiehe@stu.xjtu.edu.cn; yukunzhang@stu.xjtu.edu.cn; yuqiwei@xjtu.edu.cn).

Digital Object Identifier 10.24295/CPSSTPEA.2025.00043

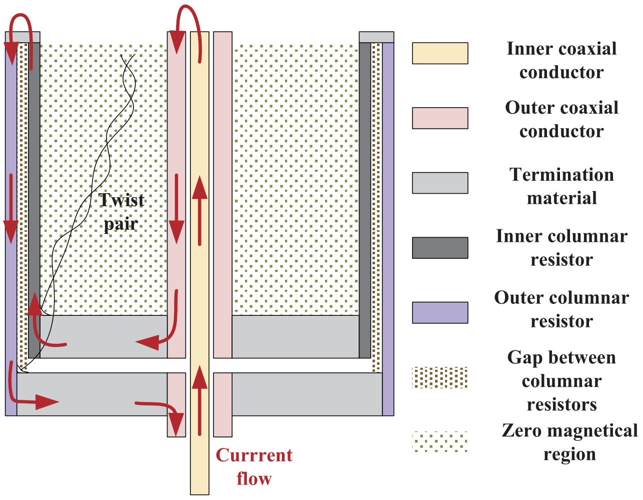

Fig. 1. Structure of a CCS [15].

of the current measurement range. For example, the 100 mΩ CCS from T&M research product (SSDN-10) could achieve a bandwidth of 2 GHz, while the current measurement range is only up to 100 A (I_{peak}) since the maximum measurement voltage is limited to ± 5 V. Especially for the turn-on moment, a very high current overshoot occurs, which is even twice larger than the static current. Such a small current measurement range make it unsuitable for a high current test. Several self-made printed circuit board (PCB)-based CCSs with high bandwidth is shown in [7], [16], [17]. However, not only a careful design required, but also an accurate simulation needs to be carried out. In order to achieve high performance, the PCB design needs several iterations to tune the tiny parasitic parameters. In addition, the self-designed CCS are not as mature as commercial ones which also makes the 'high bandwidth' unconvincing. The vector network analyzer (VNA) is also required to verify the performance of the design. So far, the CCS measurement is generally accepted to measure the current of the WBG device for researchers and suppliers. Therefore, compensating the low-resistance CCS is the best way to achieve a high current measurement range and high bandwidth simultaneously.

There are mainly two methods to compensate a CCS: 1) The hardware-based method; 2) The software-based method. The hardware-based method is to design a compensation chain or an active filter to extend the bandwidth of the CCS [14], [18]. The software-based method is to design a virtual software filter to rebuild the actual waveform of the current [15]. Nevertheless, both the hardware-based method and the software-based method require to obtain the transfer function precisely via the VNA. However, there are mainly two disadvantages for using a VNA: 1) the S-parameters matrix is sensitive to the test environment and procedure, which cannot be obtained precisely; 2) it is a very expensive equipment [19]. For example, the price of a 3 GHz VNA is around $30,000.

The structure of a classic CCS is shown in Fig. 1, and the equivalent circuit is unveiled in Fig. 2 [20]. The current flow complies well with the rule of magnetic cancellation, which minimizes the parasitic inductance of the power loop (L_{pwr}) introduced by CCS. One of the main reasons for restricting the high-bandwidth application of the common current shunt is the large inductance of the measurement loop. The CCS is an excellent solution to control the mutual inductance of the measurement loop by isolating the power loop and the measurement loop. An zero magnetic region is created between the outer coaxial conductor and the inner columnar resistor, the measurement signal is fed via this region by a low inductance twist pair [21]. As a result, the measurement loop inductance can be minimized.

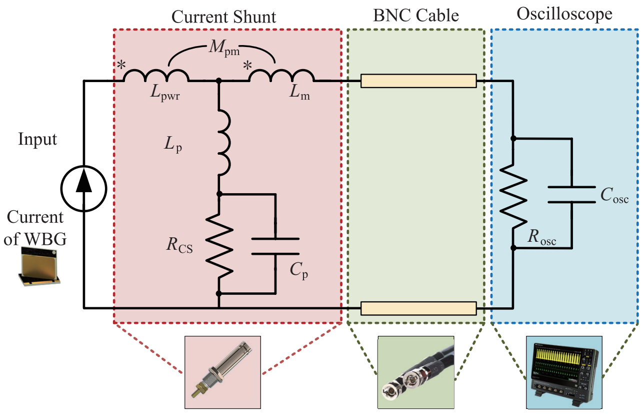

Fig. 2. Equivalent circuit of the resistive CCS measurement system.

To further improve the bandwidth of the shunt resistor, the inherent parasitic of the CCS should be given special consideration. Fig. 2 is a classical equivalent circuit used to analyze the bandwidth of the CCS. The bandwidth is approximately calculated with (1).

$$f_{\text{cutoff}} = \frac{R_{\text{CCS}}}{2\pi L_{\text{p}}} \tag{1}$$

where f_{cutoff} is the cutoff frequency of the CCS, R_{CCS} is the resistance of the CCS, L_{p} is the inherent inductance of the CCS. For CCS, several tens of nH are large enough to completely change the bandwidth characteristics [14].

There are some other factors like wave reflection due to impedance mismatch will also cause the waveform distortion, in other words, a low bandwidth [22]. However, according to [23], the attribute of the coaxial cable cannot be ignored as well. For a commonly used RG58 coaxial cable with a 0.9 mm inner diameter and 2.95 mm outer diameter, the capacitance and the inductance per unit are 100 pF and 250 nH, respectively. When the measured frequency exceed 10 MHz, the impedance measured by RG58 cannot be regarded as that measured without RG58.

Above all, the accurate model of the CCS measurement system is more complex than the classical equivalent circuit, and extracting all of those parameters is a time-consuming job. In addition, the values of these parameters are always very small, so that any slight interference might cause a considerable deviation of the results [15]. Although compensation methods do not need an model of CCS, the accurate transfer function is necessary for compensation. Only a high-cost VNA could measure the transfer function from several hertz to gigahertz.

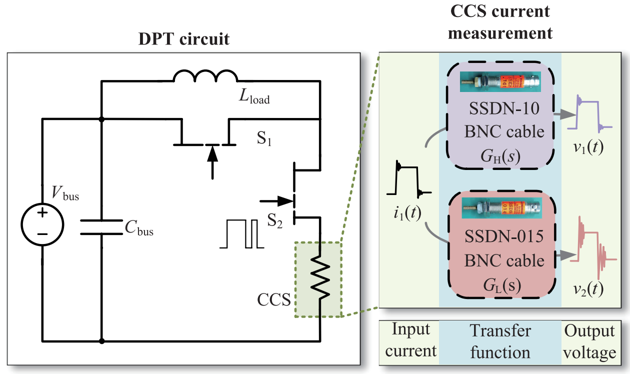

Fig. 3. DPT current measurement with the high-bandwidth CCS and the low-bandwidth CCS.

In addition, a self-designed test fixture for CCS is required, which would affect the accuracy directly.

To address the above-mentioned issues, this paper introduces an easy-to-implement software-based method to extend the bandwidth of the off-the-shelf low-resistance CCS. For this method, all instruments and equipment used are common. As a software compensation method, no complex design or operation is required. The contribution and main work of this article can be summarized as follows: 1) an easy-to-implement software based compensation method is proposed for extending the bandwidth of a low-resistance CCS to satisfy the requirement of high bandwidth and wide current measure-ment range simultaneously for WBG device characterization; 2) a comprehensive comparison is conducted among various current measurement methods, demonstrating the effectiveness of the proposed method.

The remainder of this paper is organized as follows. Section II introduces the software-based compensation method. The method is verified by experiment, and the performance of this compensation method is demonstrated in Section III. Moreover, a detailed comparison of different current measurement method is carried out. Finally, the last section concludes this paper.

II. The Proposed Software-Based Method to Compensate the Low-Resistance Current Shunt

Based on the circuit model, this section briefly introduces an easy-to-implement software-based compensation method. Bandwidth compensation can be achieved without a specific transfer function and high-cost VNA.

The CCS is usually the best choice for the WBG devices characterizations. Its high bandwidth and small parasitics meet the measurement requirement. For the same test, the current flows through the CCS is regarded as the same, while the measurement deviation of the low-resistance CCS is even greater than 30% when compared with the high-resistance CCS. Thus, compensating the low-bandwidth CCS is a critical issue for DPT in evaluating the performance of WBG devices.

Based on the analysis, the measurement systems can be regarded as a two-port network, as Fig. 3 shows. The input is the device current, and the output is the CCS voltage drop. As a linear time-invariant system, there is a transfer function (G_{vi}) from the input to the output of the CCS and the cable.

$$G_{vi}(s)=\frac{V_m(s)}{i_p(s)}=G_{CCS}(s)G_{cable}(s)G_{osc}(s) \tag{2}$$

where $G_{vi}(s)$ is the transfer function of the CCS measurement system, i_p is the actual power loop current, $G_{CCS}(s)$, $G_{cable}(s)$, and $G_{osc}(s)$ are the transfer function of the CCS, BNC cable and oscilloscope, respectively.

According to the analysis of the equivalent circuit, the CCS could be regarded as a high-pass filter. Therefore, the bandwidth of the CCS is defined by the +3 dB point of G_{vi}. With the known transfer function, a compensation transfer function ($G_{cmp}(s)$) can be designed to extend the bandwidth of the CCS. From (3), i_p could be rebuilt by $G_{cmp}(s)$. Theoretically, if $G_{cmp}(s)$ times $G_{vi}(s)$ equals 1, the frequency response is a constant value and the bandwidth of the CCS is infinite. However, to some extent, the higher the bandwidth needed for CCS, the more accurate $G_{vi}(s)$ is demanded, which always means a higher cost. As a consequence, there is a trade-off between bandwidth and cost, while compensating a CCS by $G_{vi}(s)$.

$$\begin{aligned} i_{cmp}(s) &= i_m(s)G_{cmp}(s)=i_p(s)G_{ii}(s)G_{cmp}(s)\\ &=\frac{V_m(s)G_{cmp}(s)}{R_{CCS}}\\ &=\frac{i_p(s)G_{vi}(s)G_{cmp}(s)}{R_{CCS}} \end{aligned} \tag{3}$$

where i_{cmp} is the current after compensating, $i_m(s)$ is the current measured by oscilloscope, $G_{cmp}(s)$ is the compensation transfer function, $G_{ii}(s)$ is the current transfer function of the CCS measurement system, V_m is the current measured by the oscilloscope, R_{CCS} is the nominal resistance of the CCS.

As mentioned above, the bandwidth of the CCS is determined by the consistency between $G_{ii}(s)$ and $\frac{1}{G_{cmp}(s)}$. However, the infinite-bandwidth condition does not exist in practice. The actual bandwidth is determined by the transfer function of the measurement-compensation system:

$$\begin{aligned} G_{after.cmpL}(s) &= G_{viL}(s)G_{cmpL}(s)\\ &=\frac{i_{cmpL}(s)}{i_p(s)}R_{CCS}\\ &=\frac{i_{mL}(s)}{i_{mH}(s)}G_{cmpL}(s)G_{viH}(s) \end{aligned} \tag{4}$$

where $G_{after.cmpL}(s)$ is the transfer function of the low-bandwidth CCS measurement-compensation system, G_{viL} and G_{cmpL} are the transfer function and compensation transfer function of the low-bandwidth-CCS measurement system respectively, i_{cmpL} is the low-bandwidth CCS measured current after compensation, i_{mL} and i_{mH} are the current measured by low-bandwidth and high-bandwidth respectively, G_{viH} is the transfer function of the high-bandwidth CCS.

If G_{cmpL} equals $\frac{i_{mH}(s)}{i_{mL}(s)}$, the transfer function after compensation of the low-bandwidth CCS measurement systems is de-

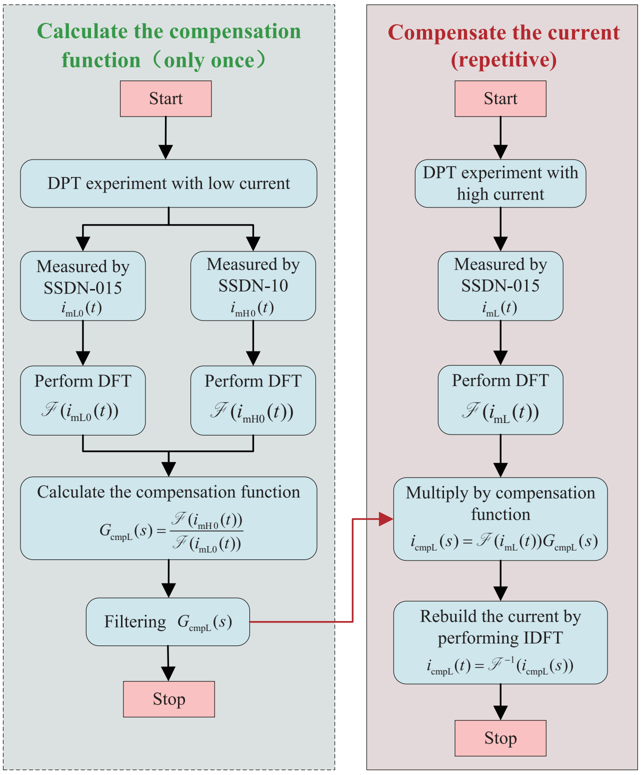

Fig. 4. Flowchart of (the proposed compensation method.

termined by that of the high-bandwidth CCS ($G_{viH}(s)$). It is the highest bandwidth can be obtained without additional equipment.

For the experiment, the current waveforms ($i_{mL}(t)$, $i_{mH}(t)$) are first acquired by a high-bandwidth CCS and a low-bandwidth CCS by a same test, respectively. The compensation function is obtained by dividing the Discrete Fourier Transform (DFT) result of $i_{mL}(t)$ and $i_{mH}(t)$. The compensation transfer function covers the frequency range from 0 Hz to the Nyquist frequency of the oscilloscope (e.g., 5 GHz for the oscilloscope with 10 GSa/s sampling rate). Meanwhile, the resolution is determined by the length of the current waveform. Both a higher sample frequency and a larger memory depth will help to improve the accuracy of the compensation transfer function. It is worthy noting that the valid compensation bandwidth is determined by the oscilloscope channel. Therefore, in this method, the compensation beyond the bandwidth of the oscilloscope will be ignored. Since the voltage signal detected by the oscilloscope is amplified according to the resistance of the CCS, the G_{ii} of the CCSs are the same in low frequency area. The only difference is that the gain of the low-bandwidth G_{iiL} is higher than the high-bandwidth G_{iiH}. On the basis of this, the formula $\frac{i_{mH}(s)}{i_{mL}(s)}$ is less than 1. Therefore, the anomalous gains of the compensation transfer function greater than 1 are set to 1 to reduce the noise of the rebuilt current waveforms.

$$\begin{aligned} i_{cmpL}(t) &= \mathscr{F}^{-1}(\mathscr{F}(i_{mL}(t))G_{cmpL}(s)) \\ &= \mathscr{F}^{-1}\left(\mathscr{F}(i_{mL}(t))\frac{\mathscr{F}(i_{mH0}(t))}{\mathscr{F}(i_{mL0}(t))}\right) \end{aligned} \tag{5}$$

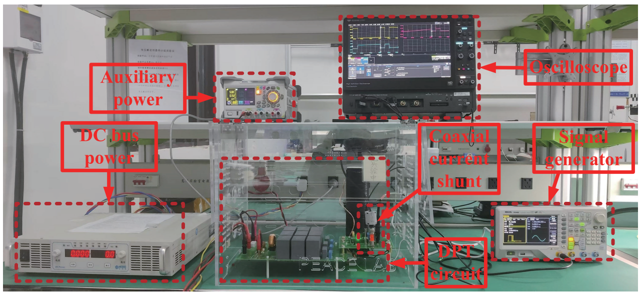

Fig. 5. DPT experiment setup.

where $\mathscr{F}$ and $\mathscr{F}^{-1}$ is the DFT and Inversed Discrete Fourier Transform (IDFT), i_{mL} is the current measured by the low-bandwidth CCS, i_{mH0} and i_{mL0} is the current measured by the high-bandwidth CCS and the low-bandwidth CCS with a same i_p.

The low-bandwidth CCS current waveform is rebuilt by the compensation transfer function according to (5). As a result, a more accurate current waveform will be obtained.

Since the compensation transfer function is extracted from the experimental waveforms, the dominant frequency for the experimental result is identified and compensated. There will be a great improvement for the accuracy of the device current.

Fig. 4 illustrates steps to carry out the proposed compensation method. Before implementing the current compensation algorithm, the compensation function $G_{cmpL}(s)$ should be obtained: 1) Measure The DPT current waveforms by SSDN-10 (i_{mH0}) and SSDN-015 (i_{mL0}) under a same DPT condition with a low current ($i_{peak} \leqslant 100$ A); 2) Performing DFT on two current waveforms; 3) Divide the DFT result of i_{mH0} by that of i_{mL0} and filter out unreasonable points. Theoretically, the extraction of the compensation function ($G_{cmp}(s)$) is needed only once, because $G_{cmp}(s)$ is just related to the CCS itself. In other words, the compensation function does not change with DPT conditions varying (e.g., voltage, current, switching speed and so on).

When the $G_{cmp}(s)$ is obtained, any current waveform measured by SSDN-015 can be compensated. 1) Perform DFT on the current measured by SSDN-015; 2) Multiply the DFT result by $G_{cmp}(s)$; 3) Rebuild the current by performing IDFT on $i_{cmpL}(s)$. It is a fixed mapping process in frequency domain according to the transfer function, therefore the current compensation is only related to $G_{cmpL}(s)$.

III. Experimental Results

A. Test Setup

To validate the proposed compensation method, a DPT experiment is carried out with two CCSs with different resistance and bandwidth. They are SSDN-10 (100 mΩ) and SSDN-015 (15 mΩ) from T&M with nominal bandwidths of 2.0 GHz and 1.2 GHz, respectively. Due to the maximum voltage of the 50 Ω channel of the oscilloscope is 5 V, the maximum current that could be measured is 100 A for SSDN-10 and 666 A for SSDN-015.

Fig. 5 shows the DPT setup, which mainly includes an oscil-

TABLE I
COMPONENT OF DPT

Component	C_{bus}	L_{load}	DUT	Driver
Value	370.5 μF	208 μH	–	–
Series	C3D3A406 FV32N103J	–	GS66516T	SI-8271GB
Vendor	faratronic PSA	self-made	Infineon	SILICON LABS
Category	PP film C0G	air core	GaN HEMT	CMOS

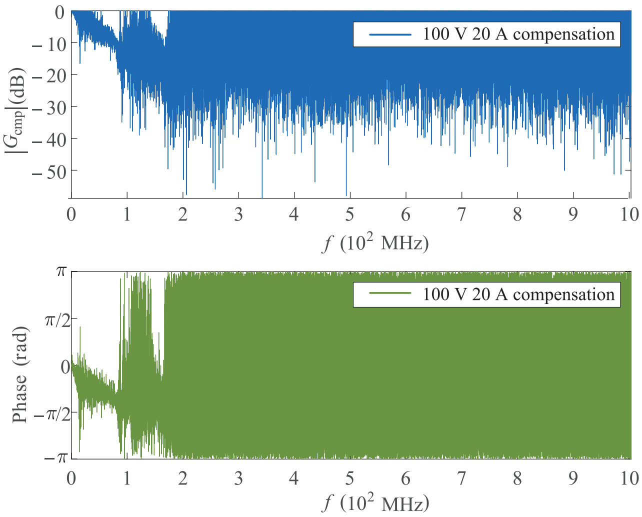

Fig. 6. Bode diagram (0–1 GHz) of the compensation transfer function.

loscope (Teledyne HDO-6104B-MS 1 GHz 10 GSa/s), a signal generator (RIGOL DG4062), an auxillary power (RIGOL DP932U) and a DC bus power supply. The voltage probe used to measure V_{ds} of S_2 is PPE6KV-A (2000V_{rms} 500 MHz) from Lecroy. The rest components is listed in TABLE I.

Since the bus voltage and pulse width to drive S_2 are changeable, different voltage and current test conditions can be tested. Two sets of drive resistors are tested to mimic scenarios with different switching speeds. The rise time of the current under the condition of 10 Ω (turn-on) / 2 Ω (turn-off) is around 10 ns which is consistent with GaN's theoretical switching speed. Another is 20 Ω (turn-on) / 10 Ω (turn-off) for the lower switching speed.

B. DPT Waveforms After Compensation

The DPT results mainly include the high voltage and high current conditions to evaluate the accuracy of high current compensation when the current is greater than 45 A (I_{peak}).

Two current waveforms measured by SSDN-10 and SSDN-015 from a same DPT experiment are obtained. The compensation transfer function is extracted by dividing the DFT of the current waveform of SSDN-10 by that of SSDN-015. Fig. 6 is the bode diagram (0 Hz–1 GHz) of the compensation transfer function ($G_{cmp}(s)$) derived from 100 V/20 A R_{on}=10 Ω R_{off}= 2 Ω DPT experiment. After processing by the filtering method introduced in Section II, the compensation transfer function is applied to compensate the current waveforms of SSDN-015. The compensated current waveform in frequency domain is calculated by multiplying $G_{cmp}(s)$ by the DFT of the waveform measured via SSDN-015. Finally, the compensated current in the time domain $i_{cmp}(t)$ is obtained by the IDFT of $i_{cmp}(s)$ as (5) in Section II.

Fig. 7 displays the waveforms under the 300 V/45 A R_{on} = 10 Ω R_{off} = 2 Ω condition and the compensated current waveform of SSDN-015. When S_2 is on, a high current overshoot occurs due to the charge of the output capacitor of S_1. Although the rated current is around 26 A, the peak current rises to 59.90 A for SSDN-015 and 45.55 A for SSDN-10. There is a much higher current overshoot and a much lower current rise time measured by SSDN-015 than that of SSDN-10. Meanwhile, a higher oscillation magnitude and phase shift are also detected after the current falls below the rated current. It also proves that the distortion of the current waveform is caused by the low bandwidth of the CCS, because the voltage waveforms between the drain and the source remains constant with different CCSs. The reason why low-bandwidth CCS contributes to this phenomenon was analyzed in Section II.

The rebuilt current waveform of SSDN-015 is also shown in Fig. 7 with the solid green line. The waveform of SSDN-10 (solid red line) and the waveform of compensated SSDN-015 are almost identical. It further proves that the difference of waveforms come from the inaccuracy of the measurement system, in other words, the CCS itself. Owing to a high bandwidth of SSDN-10, the current waveforms of SSDN-10 could be regarded as the actual current flows through the CCS. It indicates that the proposed compensation method can rebuild the actual current based on the measurement.

Furthermore, the waveforms of power dissipation are also demonstrated to evaluate the accuracy of the proposed method. The energy loss during the turn-on transient is calculated by integrating the voltage and current waveforms. A 31.62% deviation take place while measuring by SSDN-015. In contrast, there is only a deviation of 0.73% after compensation. The same conclusion could be drawn in the turn-off transient.

Fig. 8 shows the condition of 400 V/45 A (I_{peak}) R_{on}=10 Ω R_{off} =2 Ω. With the voltage rising to 400 V, the current waveforms and voltage waveforms changed and as a result the E_{on} and E_{off} have also increased than that of 300 V, the rebuilt SSDN-015 waveform still keeps good consistency with SSDN-10. It tells that the compensation function shows a linear time-invariant property which does not change with different current and voltage.

To have a different switching speed result, Fig. 9 demonstrates the condition of the 400 V/45 A (I_{peak}) R_{on}=20 Ω R_{off} =10 Ω. By increasing the drive resistor, the switching speed becomes slower, and as a consequence the switching loss gets larger. The compensation transfer function is derived from 100 V/20 A R_{on}=10 Ω R_{off}=2 Ω DPT experiment. Although the switching speed changes, the current waveform can also be well compensated.

A wide range of current measurement is the main reason

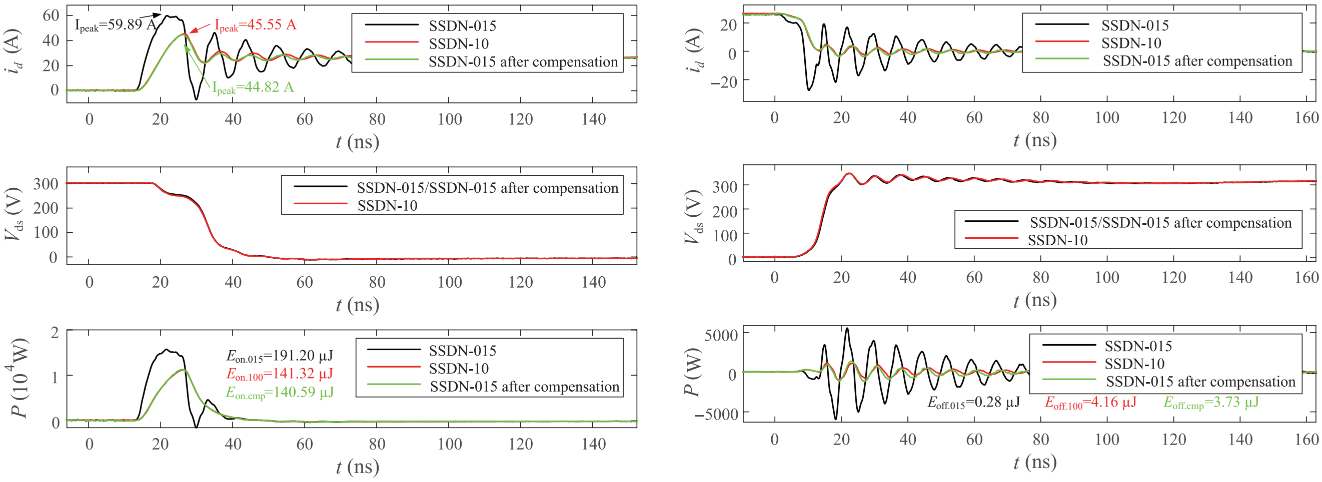

(a) (b)

Fig. 7. 300 V 45 A (I_{peak}) R_{on}=10 Ω R_{off}=2 Ω DPT waveform compensation results using 100 V 20 A (I_{peak}). (a) Turn-on waveforms and power loss, (b) Turn-off waveforms and power loss.

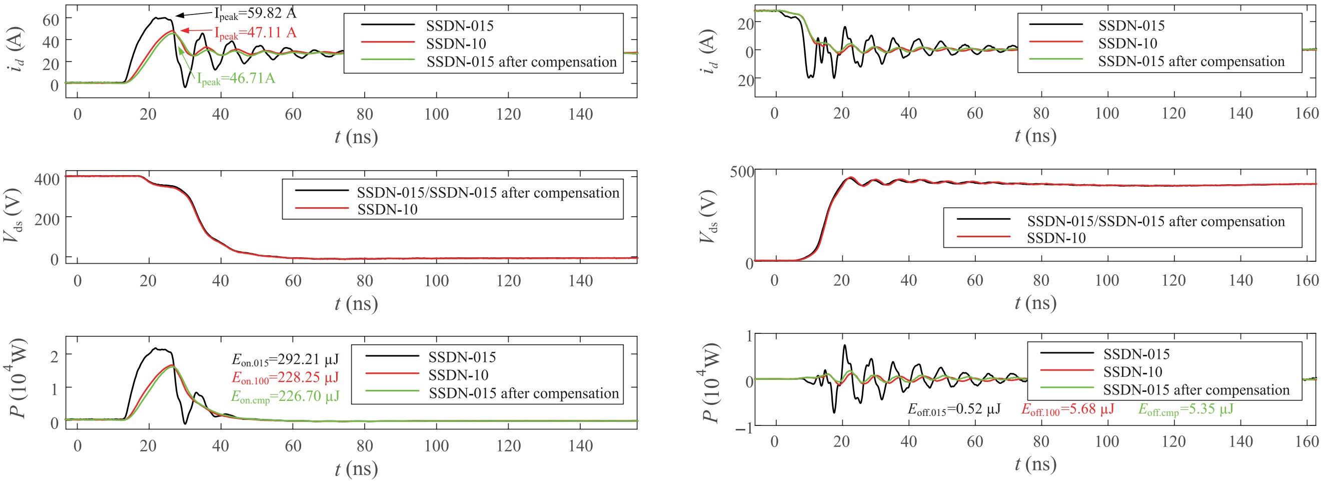

(a) (b)

Fig. 8. 400 V 45 A (I_{peak}) R_{on}=10 Ω R_{off}=2 Ω DPT waveform compensation results using 100 V 20 A (I_{peak}). (a) Turn-on waveforms and power loss, (b) Turn-off waveforms and power loss.

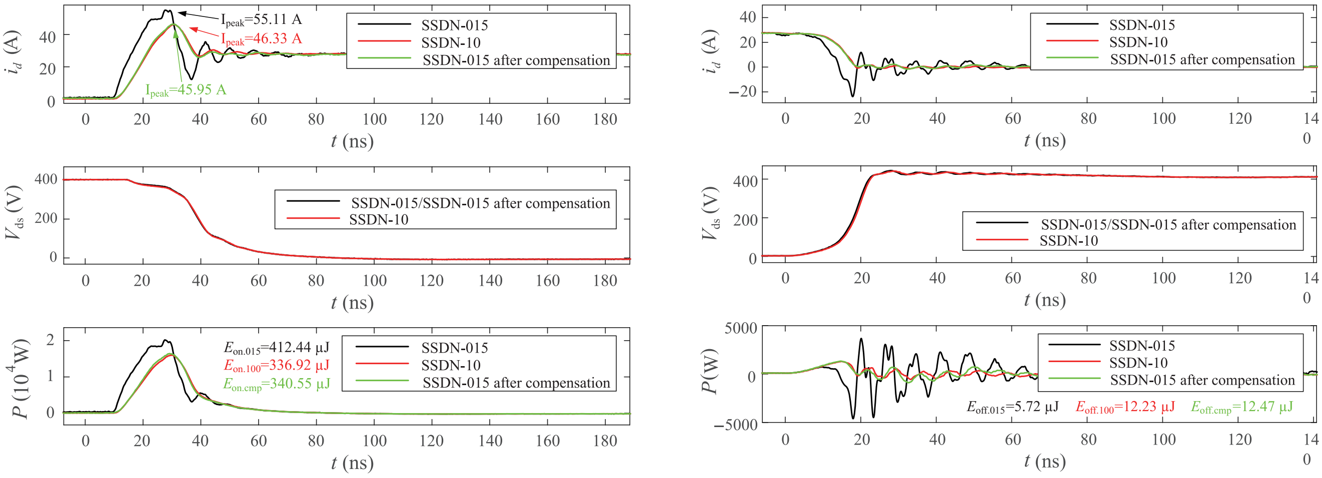

(a) (b)

Fig. 9. 400 V 45 A (I_{peak}) R_{on}=20 Ω R_{off}=10 Ω DPT waveform compensation results using 100 V 20 A (I_{peak}). (a) Turn-on waveforms and power loss, (b) Turn-off waveforms and power loss.

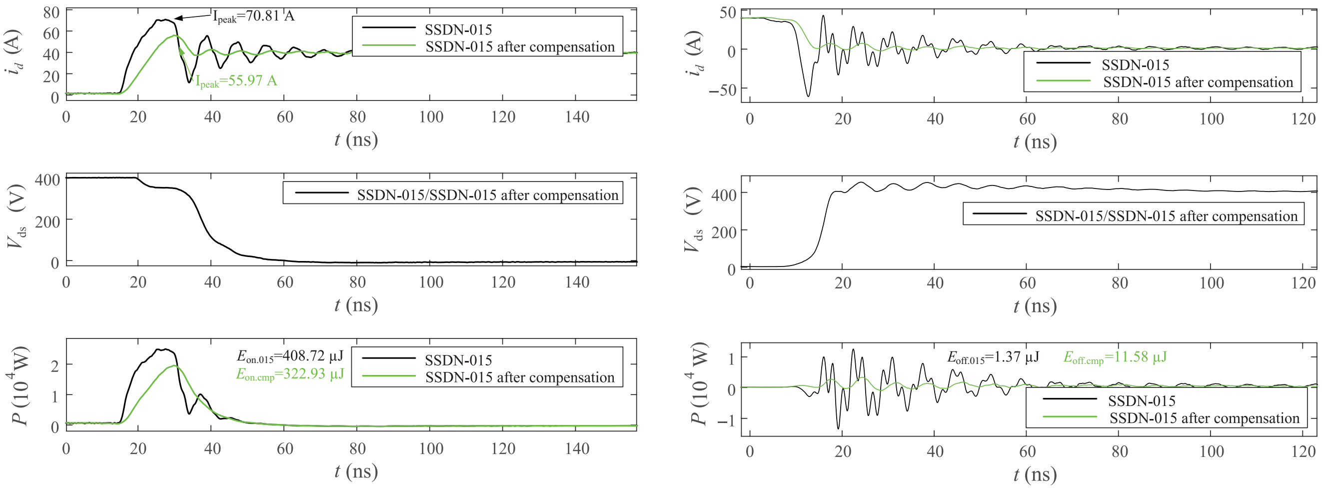

(a) (b)

Fig. 10. 400 V 60 A (I_{peak}) R_{on}=10 Ω R_{off}=2 Ω DPT waveform compensation results using 200 V 30 A (I_{peak}). (a) Turn-on waveforms and power loss, (b) Turn-off waveforms and power loss.

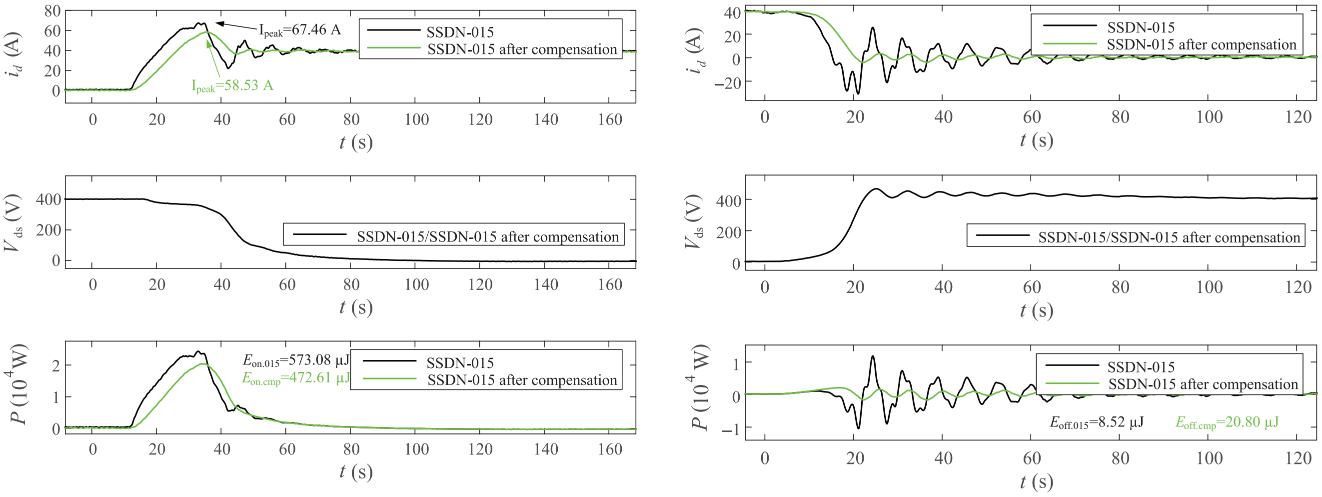

(a) (b)

Fig. 11. 400 V 60 A (I_{peak}) R_{on}=20 Ω R_{off}=10 Ω DPT waveform compensation results using 100 V 20 A (I_{peak}). (a) Turn-on waveforms and power loss, (b) Turn-off waveforms and power loss.

why the compensation of the low-resistance CCS needs to be conducted. The 400 V 60 A (I_{peak}) R_{on}=10 Ω R_{off}=2 Ω DPT waveforms is shown in Fig. 10. The compensation transfer function is derived from 100 V 20 A R_{on}=10 Ω R_{off}=2 Ω DPT. Because the peak current exceeds 50 A, the current waveform larger than 50 A of SSDN-10 is eliminated. Therefore the current of SSDN-10, which makes the result unreliable, is not shown in the diagrams. Despite the rebuilt current waveform cannot be evaluated by comparing with the current waveform of SSDN-10. It can be observed that the peak current and abnormal oscillation are well attenuated via the compensation method. By calculation, there is a 13.23% attenuation of the peak current and a 15.22% attenuation of energy loss. For turn-off, large oscillations and waveform distortions are eliminated. Instead, a smooth current waveform is obtained. The switching loss also states a correct trend, and locate in a reasonable value whether for Fig. 10 or Fig. 11.

C. Turn-On/Off Switching Loss After Compensation

A comprehensive analysis of the switching energy is listed in TABLE II. All the compensation transfer function is derived from 100 V 20 A DPT waveform. For the turn-on switching loss (E_{on}), here is a 20% error for the SSDN-015 at least. In contrast, the deviation of the compensation could always be kept below a low level less than 1.08%. However, the situation of turn-off is not as optimistic as that of switching on. There are at least 50% turn-off switching loss errors for SSDN-015. Even under a 300 V 45 A circumstance, a 98% deviation is obtained, which is unacceptable.

The compensation helps to get an accurate switching loss evaluation at switching loss test points (e.g., 400 V/45 A R_{on}=20 Ω R_{off}=10 Ω). In the low voltage DPT, there is still some deviation between the turn-off loss and the actual value (e.g., 7.93% for 300 V/45 A (I_{peak}) R_{on}=10 Ω R_{off}=2 Ω), but the deviation caused by the compensation is insignificant compared to

TABLE II
Switching Loss Results on DPT (μJ)[a]

Case	measurement	t_{rise}	t_{fall}	E_{off}	E_{on}	E_{total}	I_{peak}
300 V 45 A (I_{peak}) R_{on} =10 Ω R_{off}=2 Ω	SSDN-10	7.0(0.00%)	16.0(0.00%)	4.16(0.00%)	141.32(0.00%)	145.48(0.00%)	45.55(0.00%)
	SSDN-015	2.8(−60.00%)	7.0(−56.25%)	0.28(−93.27%)	191.20(+35.30%)	191.48(+31.62%)	59.90(+31.50%)
	Compensation	7.0(+0.00%)	15.7(−1.88%)	3.83(−7.93%)	140.59(−0.52%)	144.42(−0.73%)	44.82(−0.73%)
400 V 45 A (I_{peak}) R_{on} =10 Ω R_{off}=2 Ω	SSDN-10	7.3(0.00%)	16.9(0.00%)	5.68(0.00%)	222.57(0.00%)	228.25(0.00%)	47.11(0.00%)
	SSDN-015	3.1(−57.53%)	8.1(+52.07%)	0.52(−90.85%)	291.69(+31.06%)	292.21(+28.02%)	59.82(+26.98%)
	Compensation	7.4(+1.37%)	16.4(−2.96%)	5.35(−5.81%)	221.36(−0.54%)	226.70(−0.96%)	46.71(−0.85%)
400 V 55 A (I_{peak}) R_{on} =10 Ω R_{off}=2 Ω[b]	SSDN-10	–	–	–	–	–	–
	SSDN-015	5.3(−51.38%)	10.4(−48%)	1.37(−88.17%)	408.73(+31.27%)	410.09(+26.99%)	70.81(+26.51%)
	Compensation	10.9(0.00%)	20.0(0.00%)	11.58(0.00%)	311.36(0.00%)	322.93(0.00%)	55.97(0.00%)
300 V 45 A (I_{peak}) R_{on} =20 Ω R_{off}=10 Ω	SSDN-10	13.3(0.00%)	20.0(0.00%)	7.17(0.00%)	211.43(0.00%)	218.59(0.00%)	44.02(0.00%)
	SSDN-015	7.0(−47.37%)	14.6(−27.00%)	0.08(−98.89%)	263.60(+24.67%)	263.68(+20.63%)	52.73(+19.79%)
	Compensation	12.9(−3.00%)	21.5(+7.5%)	7.02(−2.09%)	212.05(+0.29%)	219.07(+0.22%)	43.50(−0.12%)
400 V 45 A (I_{peak}) R_{on} =20 Ω R_{off}=10 Ω	SSDN-10	12.9(0.00%)	22.9(0.00%)	12.23(0.00%)	336.92(0.00%)	349.15(0.00%)	46.33(0.00%)
	SSDN-015	7.3(−43.41%)	17.0(−25.76%)	5.72(−53.23%)	412.44(+22.41%)	418.16(+19.77%)	55.11(+18.95%)
	Compensation	12.6(−2.33%)	22.9(+0.00%)	12.47(+1.96%)	340.55(+1.08%)	353.02(+1.11%)	45.95(−0.82%)
400 V 60 A (I_{peak}) R_{on} =20 Ω R_{off}=10 Ω[b]	SSDN-10	–	–	–	–	–	–
	SSDN-015	9.3(−38.00%)	17.4(−29.89%)	8.52(−59.04%)	573.08(+21.29%)	581.60(+17.95%)	67.46(+15.26%)
	Compensation	15.0(0.00%)	22.6(0.00%)	20.80(0.00%)	472.61(0.00%)	493.10(0.00%)	58.53(0.00%)

a. All compensations are compensated with files derived from the 100 V 20 A (I_{peak}) DPT waveforms.
b. The peak current is over 50 A, exceeding the measurement range of the SDN-10, where the compensation results are regarded as the reference.

the error before compensation. These errors might come from the random error of compensation, because the value of the turn-off loss is already so small that any slight calculation error may cause a significant change of the turn-off loss. The total loss of turn-on loss transient and turn-off transient is also evaluated, an error less than 1.11% indicates that the compensation method is a proven method for the accurate evaluation of the analysis.

D. Effect Analysis for Different Compensation Transfer Functions

The bode diagram of the compensation transfer function is shown in Fig. 12. The regular attenuation is observed from 0 Hz to around 150 MHz.

This phenomenon could be seen in the third sub-figure as well, which is the DFT of $i_{\text{m}}(t)$. It indicates that the main frequency for the DPT of this article is located mainly below 150 MHz. The transfer functions derived from the 100 V 20 A R_{on} =10 Ω R_{off}=2 Ω DPT and the 100 V 20 A R_{on}=20 Ω R_{off}=10 Ω DPT is drawn in Fig. 12 simultaneously. Both the gains and the phase shifts show the same trend in the frequency domain of 0–150 MHz. It also explains that the compensation transfer function is not sensitive to the DPT condition from which it is derived.

The DPT waveforms of 300 V/30 A, 300 V/40 A, 300 V/50 A, and 300 V/60 A are compensated by three different transfer functions as shown in Fig. 13. The switching loss is calculated and arranged in the order of peak current magnitude. The transfer functions used for compensations ($E_{\text{total.cmp1}}$, $E_{\text{total.cmp2}}$, $E_{\text{total.cmp3}}$) are obtained from the 100 V/20 A, 100 V/30 A, and 200 V/30 A R_{on}=10 Ω R_{off}=2 Ω DPT. Three compensation results (I_{peak}=30 A; 40 A; 50 A) of the total switching loss all match well with the results of SSDN-10. Although the current waveform cannot be measured by SSDN-10 when I_{peak}=60 A, the compensation results with different compensation function almost keep consistent. In any current level, the switching loss deviation could be kept below 3% even under the worst condition.

In general, alone with an excellent performance on the waveform rebuilding and loss evaluation of the device, the proposed compensation method for low-resistance CCSs also shows that this method is not sensitive to the selection the transfer function.

E. Comparisons Between Current Measurement Method

Several current measurement methods either from commercial products or literature are listed and compared in TABLE III. Comparisons are carried out from different dimensions as well.

The common commercial products for power semiconductor device characterization is based on RC or CT. To evaluate the current measurement performance while characterizing WBG devices, a multi-fixture PCB was designed in Fig. 14. The only difference from Fig. 5 is the power loop which is marked in the upper view and side view. A fixture wire is welded between the divided ground panel. Therefore, the current flows through S_2

TABLE III
COMPARISON BETWEEN DIFFERENT CURRENT MEASUREMENT METHODS

Method	Reference	Bandwidth	$L^{a}_{\text{loop insertion}}$	Commercial/Laboratory	Complexity	Current range (I_{peak})
RC	[9]	50 MHz	* * **	Commercial	*	3000 A
CT	[8]	250 MHz	* * * * *	Commercial	*	100 A
Embedded planar RC	[10]	185 MHz	*	Laboratory	* * * * *	184 A
Impedance-matching shunt	[16]	⩾ 3 GHz	*	Laboratory	* * **	100 A
SMD CCS	[7]	80 MHz	*	Laboratory	* * **	500 A
SMD shunt + active compensation	[18]	1.6 GHz	**	Laboratory	* * * * *	1000 A
Passive compensation	[14]	587 MHz	*	Commercial	* * * * *	666 A
Software compensation	[15]	–	**	Commercial	* * *	100 A
Software compensation(this work)	–	≈ 1 GHz	**	Commercial	**	666 A

a. The current route is extended for current measurement, therefore the loop parasitic inductance will increase.

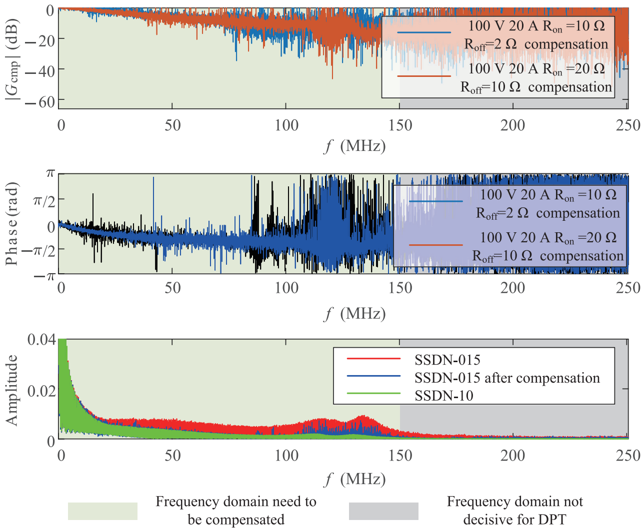

Fig. 12. Bode diagrams (0–250 MHz) of the compensation transfer function for different test condition and the DPT current waveforms in the frequency domain.

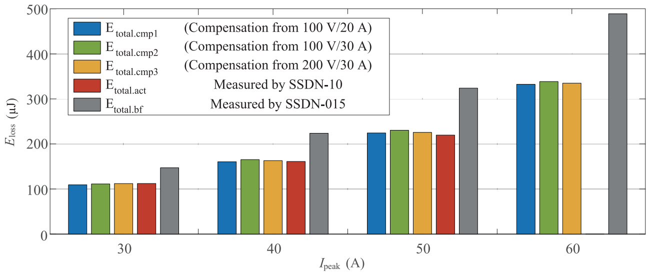

Fig. 13. Switching loss using different compensation transfer function.

can be measured by RC and CT, either.

Fig. 15 shows the DPT waveform measured by CCS (T&M SSDN-10), CT, and RC with the condition of 400 V/50 A (I_{peak}) R_{on}=20 Ω R_{off}=2 Ω. The CCS, CT, and RC are SSDN-10 (2GHz) from T&M, HCPX8070 (30 MHz) from CYBERTEK and RCP600XS (3−50 MHz) from MICSIG, respectively. Even though the current being measured is the same, the delay, the rise/fall time and the peak current are different. Because the current waveforms demonstrated in Fig. 15 is not aligned, the waveform measured by CCS can be identified with the lowest delay among three probes. The highest peak current is also measured by SSDN-10 which means a great high frequency gain. Moreover, the di/dt value measured by SSDN-10 is the largest one. During turn-off switching, the current of SSDN-10 exhibits a di/dt nearly two times larger than that observed in the CT and RC. A severe oscillation is also observed for both the RC and the CT, but not for the CCS.

Whether the peak current or the di/dt proves a worse performance of the commercial CT and RC because of its limited bandwidth. The commercial RC and CT are also not ideal probes for measuring current embedded in the PCB, because the current route must be changed for fixture which will drastically increase the loop inductance. In addition, the bandwidth of RC and CT are restricted by the integrator and the magnetic core, respectively. These reasons make the commercial CCS is still nearly the only way for WBG device characterization.

Some representative current-measurement probes made in the laboratory are also listed in TABLE III. [10] makes a PCB-embedded planar RC achieving a bandwidth of 185 MHz with a current range around 184 A. [16] proposes a new impedance matching method for bandwidth improvement and designs a 3 GHz prototype. [7] designs three SMD CCSs with different resistance and bandwidth, and the bandwidth of a 10 mΩ is only 80 MHz. Based on [7], [18] solves the low bandwidth problem with an active compensation module. Although all of the laboratory-made methods mention above obtain low loop inductance, they cannot balance the bandwidth, current measurement range and complexity. The technique itself is not yet mature, and the reliability of these laboratory-made methods cannot be guaranteed.

Compensation methods based on commercial products are also proposed. However, whether the hardware method [14] or the software [15] needs a carefully tuning with the VNA before it performs well. Therefore, the software compensation in this article not only can achieve a high bandwidth and a wide measurement range but also conducts in a more practical way with low complexity.

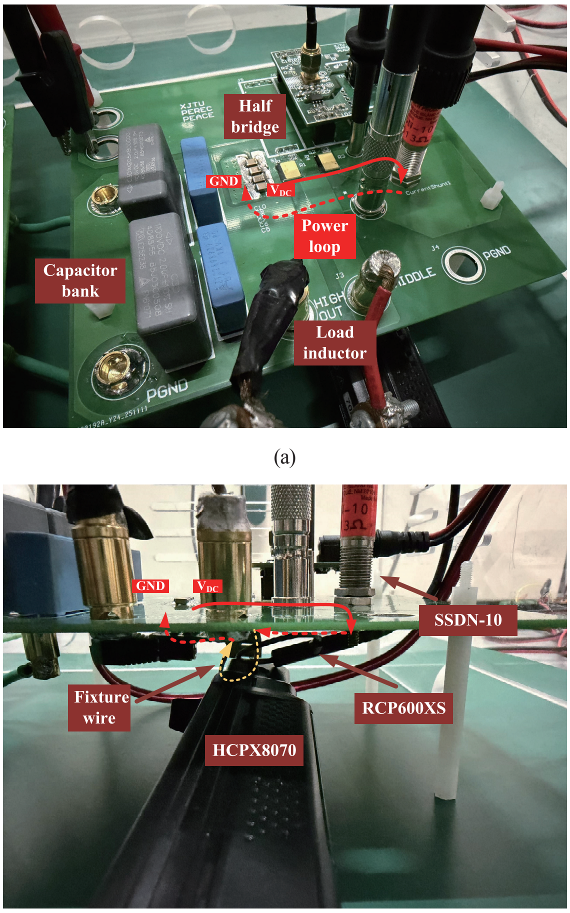

(b)

Fig. 14. Setup for current measuring with different probes. (a) Upper view, (b) Side view.

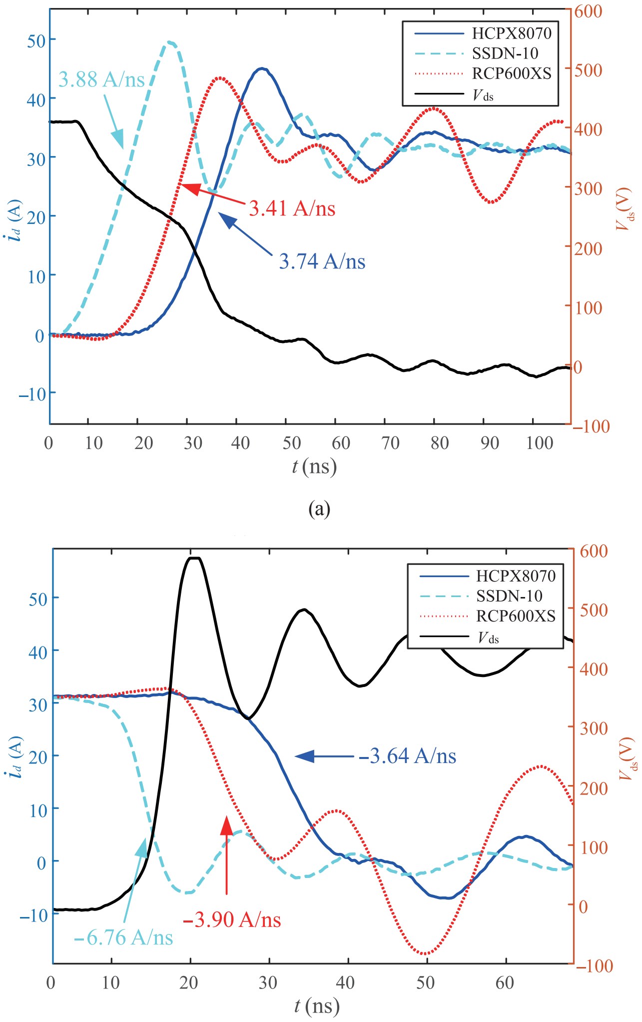

(b)

Fig. 15. 400 V 50 A (I_{peak}) R_{on}=20 Ω R_{off}=2 Ω DPT waveforms measured by different probes. (a) Turn-on waveforms, (b) Turn-off waveforms.

IV. CONCLUSION

This paper proposed a novel software-based compensation method for low-resistance CCS. Considering the CCS measurement system as a two-port network, the implementation of the proposed method is simple and stable. Only with the assistance of the high-bandwidth CCS, the compensation could be conducted. The exhibition of a high reproduction of current waveforms for the WBG device indicates the effectiveness of the method as well. The result of the switching loss prove the precision of the proposed method with only 1.11% deviation of the total switching loss. Considering about the complexity, bandwidth and product maturity, the proposed method is the optimal one compared with other current measurement methods. Above all, it is a low cost method to compensate the low-resistance CCS and acquire accurate switching loss results for WBG device characterizations.

REFERENCES

[1] U. K. Mishra, P. Parikh, and Yi-Feng Wu, "AlGaN/GaN HEMTs-an overview of device operation and applications," in *Proceedings of the IEEE*, vol. 90, no. 6, pp. 1022–1031, Jun. 2002.

[2] J. Millán, P. Godignon, X. Perpiñà, A. Pérez-Tomás, and J. Rebollo, "A survey of wide bandgap power semiconductor devices," in *IEEE Transactions on Power Electronics*, vol. 29, no. 5, pp. 2155–2163, May 2014.

[3] E. A. Jones, F. Wang, D. Costinett, Z. Zhang, and B. Guo, "Temperature-dependent turn-on loss analysis for GaN HFETs," in *2016 IEEE Applied Power Electronics Conference and Exposition (APEC)*, Long Beach, CA, USA, 2016.

[4] J. Gareau, R. Hou, and A. Emadi, "Review of loss distribution, analysis, and measurement techniques for GaN HEMTs," in *IEEE Transactions on Power Electronics*, vol. 35, no. 7, pp. 7405–7418, Jul. 2020.

[5] E. A. Jones, F. F. Wang, and D. Costinett, "Review of commercial GaN power devices and GaN-based converter design challenges," in *IEEE Journal of Emerging and Selected Topics in Power Electronics,* vol. 4, no. 3, pp. 707–719, Sept. 2016.

[6] Z. Zhang, L. M. Tolbert, D. Costinett, F. Wang, and B. J. Blalock, "A new hands-on course in characterization of wide-bandgap devices," in *IEEE Transactions on Power Electronics*, vol. 34, no. 10, pp. 9392–9403, Oct. 2019.

[7] W. Zhang, Z. Zhang, F. Wang, E. V. Brush, and N. Forcier, "High-bandwidth low-inductance current shunt for wide-bandgap devices dynamic characterization," in *IEEE Transactions on Power Electronics*, vol. 36, no. 4, pp. 4522–4531, Apr. 2021.

[8] Pearson Electronics, Inc., *Model 6600 Current Monitor Operating Manual*, Sunnyvale, CA, USA, Manual 6600, 2020. [Online]. Available: https://www.pearsonelectronics.com/pdf/7713-03.pdf.

[9] Power Electronics Measurement Ltd., "CWT miniHF rogowski current

transducers," PEM Ltd., Datasheet, 2020. [Online]. Available: https://www.pemuk.com/.

[10] M. Spieler, C. -W. Chang, A. M. El-Refaie, D. Dong, and R. Burgos, "Design of a high-bandwidth compact DC-bus embedded planar rogowski coil for SiC MOSFET current sensing," in *IEEE Transactions on Power Electronics*, vol. 39, no. 12, pp. 16482–16497, Dec. 2024.

[11] X. Zhao, R. Phukan, C. -W. Chang, R. Burgos, P. Asfaux, S. Uicich, and D. Dong, "Design of ultracompact gate driver integrated with current sensor and commutation path for a 211-kW three-level SiC aircraft propulsion inverter," in *IEEE Journal of Emerging and Selected Topics in Power Electronics*, vol. 11, no. 4, pp. 4077–4094, Aug. 2023.

[12] S. B. Sohid, X. Tian, N. Jia, H. Cui, W. Zhang, F. Wang, and B. Holzinger, "PCB rogowski coil with DC sensing for double pulse test applications," in *IEEE Transactions on Power Electronics*, vol. 39, no. 4, pp. 4494–4502, Apr. 2024.

[13] S. Ziegler, R. C. Woodward, H. H. -C. Iu, and L. J. Borle, "Current sensing techniques: A review," in *IEEE Sensors Journal*, vol. 9, no. 4, pp. 354–376, Apr. 2009.

[14] Q. Hui, B. Li, X. Ren, and Q. Chen, "Extending current shunt bandwidth for accurate switching loss evaluation of wide-bandgap devices," in *IEEE Transactions on Power Electronics*, vol. 39, no. 11, pp. 14342–14352, Nov. 2024.

[15] W. Zhang, Z. Zhang, and F. Wang, "Review and bandwidth measurement of coaxial shunt resistors for wide-bandgap devices dynamic characterization," in *2019 IEEE Energy Conversion Congress and Exposition (ECCE)*, Baltimore, MD, USA, 2019, pp. 3259–3264.

[16] Y. Wang, Z. Zeng, T. Long, P. Sun, L. Wang, and M. Zou, "Impedance-matching shunt: Current sensor with ultrahigh bandwidth and extremely low parasitics for wide-bandgap device," in *IEEE Transactions on Power Electronics*, vol. 37, no. 10, pp. 11528–11533, Oct. 2022.

[17] L. Shillaber, L. Ran, Y. Shen, and T. Long, "Gigahertz current measurement for wide band-gap devices," in *2020 IEEE Energy Conversion Congress and Exposition (ECCE)*, Detroit, MI, USA, 2020, pp. 2357–2363.

[18] L. Shillaber, Y. Jiang, L. Ran, and T. Long, "Ultrafast current shunt (UFCS): A gigahertz bandwidth ultra-low-inductance current sensor," in *IEEE Transactions on Power Electronics*, vol. 37, no. 12, pp. 15493–15504, Dec. 2022.

[19] S. Klever, A. Thönnessen, and R. W. De Doncker, "Characterization of conventional and advanced current measurement techniques suitable for WBG semiconductor devices," in *2022 24th European Conference on Power Electronics and Applications (EPE'22 ECCE Europe)*, Hanover, Germany, 2022, pp. P.1–P.10.

[20] C. M. Johnson, "Current measurement using compensated coaxial shunts," in *1991 IEE Colloquium on Measurement Techniques for Power Electronics*, London, UK, 1991, pp. 7/1–7/4.

[21] J. A. Ferreira, W. A. Cronje, and W. A. Relihan, "Integration of high frequency current shunts in power electronic circuits," in *PESC '92 Record. 23rd Annual IEEE Power Electronics Specialists Conference*, Toledo, Spain, 1992, pp. 1284–1290.

[22] J. B. Mendez, M. J. Freire, and M. A. M. Prats, "Overcoming the effect of test fixtures on the measurement of parasitics of capacitors and inductors," in *IEEE Transactions on Power Electronics*, vol. 35, no. 1, pp. 15–19, Jan. 2020.

[23] D. M. Pozar, *Microwave engineering: theory and techniques*. John Wiley & Sons, 2021.

Zilong Chen received the B.S. degree in Electrical Engineering from Northeastern University, Shenyang, China, in 2022. He is currently working toward the Ph.D. degree in electrical engineering at Xi'an Jiaotong University, Xi'an, China.

His research interests include the Gallium Nitride power semiconductor devices and cryogenic power electronics.

Yanjie He received the B.S. degree in Electrical Engineering from Xi'an Jiaotong University, Xi'an, China, in 2023. He is currently working toward the M.S. degree in electrical engineering at Xi'an Jiaotong University, Xi'an, China, and with Politecnico di Milano, Milan, Italy.

His research interests include the modeling of wide bandgap devices and its applications.

Yukun Zhang received the B.S. degree in Electrical Engineering from the University of Electronic Science and Technology of China, Chengdu, China, in 2024. He is currently working toward the M.S. degree in electrical engineering at Xi'an Jiaotong University, Xi'an, China.

His current research interests include wide-bandgap power semiconductor devices and their cryogenic characteristics.

Yuqi Wei was born in Henan, China, in 1995. He received his B.S. degree in Electrical Engineering from Yanshan University, Hebei, China, in 2016, and his M.S. degree in Electrical Engineering from University of Wisconsin-Milwaukee (UWM), Wisconsin, U.S.A., in 2018. He received a second M.S. degree in Electrical Engineering from Chongqing University, Chongqing, China, in 2019. He was a Visiting Researcher with Kiel University, Germany from September to December 2021. He received his Ph.D. degree in Electrical Engineering from the University of Arkansas, Fayetteville, U.S.A., in 2022. He was a Postdoctoral Researcher at University of Arkansas in 2022. Since 2023, he has been a Full Professor with Xi'an Jiaotong University.

His current research interests include wide band gap devices, design automation, and cryogenic power electronics.